JOURNAL OF GEOPHYSICAL RESEARCH, VOL. 102, NO. D14, PAGES 17,015–17,022, JULY 27, 1997

Determination of aerosol optical depth and land surface directional reflectances using multiangle imagery

John V. Martonchik
Jet Propulsion Laboratory, California Institute of Technology, Pasadena, California

Abstract. Spectral aerosol optical depths, surface hemispherical-directional reflectance factors, and bihemispherical reflectances (albedos) are retrieved for an area of Glacier National Park using spectral, multiangle imagery obtained with the airborne advanced solid state array spectroradiometer (ASAS). The retrieval algorithms are described and are identical in principle to those being devised for use by the multiangle imaging spectroradiometer (MISR) which will fly on the EOS-AM1 spacecraft in 1998. As part of its science mission, MISR will produce global coverage of both aerosol amounts and land surface reflection properties. The results in this paper represent the initial effort in applying the MISR algorithms to real data. These algorithms will undergo additional testing and validation as more multiangle data become available.

1. Introduction

Knowledge of aerosol characteristics and surface reflection properties on a global basis are essential inputs to the study of atmospheric and biospheric climate processes [*Charney et al.*, 1977; *Dickinson*, 1983; *Mintz*, 1984]. The multiangle imaging spectroradiometer (MISR) is a radiometrically calibrated instrument, scheduled for launch in 1998 on the EOS-AM1 spacecraft, which will provide such information in a routine manner [*Diner et al.*, 1991]. It has nine CCD pushbroom cameras to provide images at angles of 70.5°, 60.0°, 45.6°, 26.1°, and 0° relative to nadir, both forward and aftward along the direction of flight. Each camera observes continuously in four spectral bands (443, 555, 670, and 865 nm) and in the global coverage mode will produce imagery with a spatial sampling of 1.1 km and global coverage within 9 days. Operating at an altitude of about 705 km and in a polar orbit, all nine cameras will observe the same ground point within 7 min, guaranteeing that essentially identical atmospheric conditions will exist for each scene viewed at the nine different angles.

To test and validate the aerosol and surface retrieval algorithms which will be used by MISR adequately, it is necessary to have comparable, radiometrically calibrated multiangle imagery. Spacecraft data sets currently available are not well suited to this purpose. Advanced very high resolution radiometer (AVHRR) data, for example, have a footprint size of about 1 km at nadir, similar to that of MISR, but only in a single spectral channel in the visible and one in the near infrared. More importantly, since AVHRR is a cross-track scanning instrument, a set of images of a given region covering a wide range of view angles (up to 55°) can only be obtained using data from different days. An undesirable consequence, for the purpose of testing MISR algorithms, is that each image is probably produced under different atmospheric conditions. ATSR-2 onboard ERS-2 also has a nadir footprint of about 1 km and has two spectral channels (0.65 and 0.85 μm) similar to MISR channels. However, it is a conical scanning instrument, producing two views of a region (one near nadir and another near 55° off nadir in the forward direction) within 2 min of each other. Images at only two view angles are insufficient to represent the range of view angles exercised by the MISR multiangle-dependent retrieval algorithms.

At present the data sets that come closest to simulating MISR-type imagery are those produced by the airborne advanced solid state array spectroradiometer (ASAS) [*Irons et al.*, 1991]. Contiguous spectral bands cover the wavelength region 400–1000 nm and view angle coverage ranges from 70° forward to 55° aftward. The spatial resolution, however, is about 4 m at a typical observing altitude of 5 km, considerably higher than for MISR, and the areal extent of coregistered ASAS scene imagery at the various view angles is of the order of 1 km^2, about equal in size to a single MISR pixel. Nevertheless, the MISR algorithm for aerosol optical depth retrieval can be applied to the ASAS data because the algorithm depends mainly on there being some spatial contrast within the scene and not particularly on the spatial scale. The spatial scale, however, does affect how the diffuse radiation component of the measured radiance is treated. For ASAS data the diffuse radiance is assumed to be spatially invariant (pixel independent) over the scene, whereas for MISR data, with its coarser resolution, we will assume this component to be spatially variable. Another difference is that MISR takes measurements from above the atmosphere, whereas ASAS observations are made with a nonnegligible amount of atmosphere above the aircraft. We have coded the retrieval algorithms for both aerosol optical depth and surface directional reflectances to handle both types of data.

2. ASAS Data Set Description and Preprocessing

A series of multiangle ASAS images was made of Bowman Lake in Glacier National Park, Montana, at about 1500 LT on February 26, 1992. The lake is at an elevation of 1.25 km and the aircraft flew at an altitude of 4.45 km above sea level with a heading of 235° measured clockwise from true north. The Sun was in the west at a zenith angle of 63.4° and an azimuth angle of 214°, also measured from true north. Thus the aircraft was flying in the general direction of the Sun position, only about 20° azimuth angle from the principal plane. Images at 10

Paper number 96JD02444.
0148-0227/97/96JD-02444$09.00

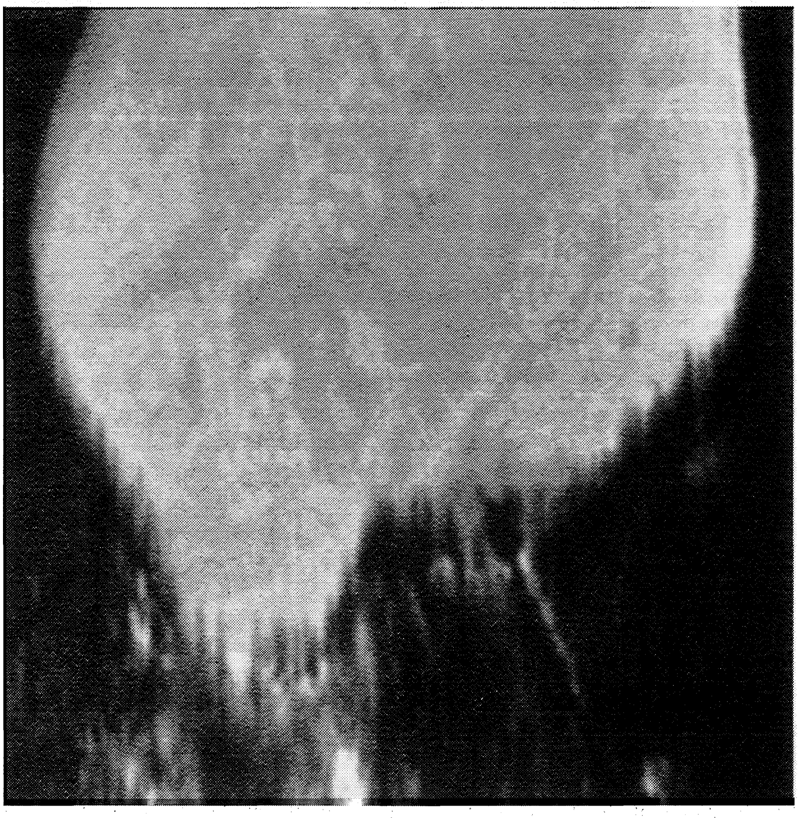

Figure 1. Advanced solid state array spectroradiometer image of Bowman Lake, Glacier NP, Montana. SW is toward the top.

different view angles (70°, 60°, 45°, 30°, and 15° in the forward look direction, nadir, and 15°, 30°, 45°, and 55° in the aftward look direction) were obtained in succession along a single flight line. The 559-nm band image with a forward look of 15° is displayed in Figure 1, showing the northeast tip of the ice- and snow-covered lake surrounded by a conifer forest.

Before the multiview angle images could be analyzed for geophysical information by the retrieval algorithms, they first had to be spatially coregistered; that is, the same pixel location in all of the images needed to correspond to the same physical point in the scene. The image coregistration process was done manually, using selected tie points to rubbersheet the off-nadir images to the nadir one. Although the ASAS instrument has an instantaneous swath width of about 2 km at nadir, the effects of aircraft roll and increasing spatial coverage with off-nadir view angle reduced the common swath observed for all 10 view directions to about a 1 km square resulting in a 256 × 256 pixel image for each view. The coregistration accuracy was generally of the order of ±0.2 pixel with a small number of localized areas misregistered by up to 1 pixel. After coregistration of the 10 view angle images for each ASAS spectral band the calibration coefficients were applied, converting digital counts to W m^{-2} sr^{-1} μm^{-1}. The resulting radiometrically calibrated images then were spatially averaged over 4 × 4 pixels to produce a final 64 × 64 pixel image data set. The pixel averaging was done to minimize any coregistration errors, to minimize variable footprint size effects at the different view angles and to increase the signal-to-noise ratio. Although the data set contained images for 29 spectral bands, only those four bands closest to the MISR bands were analyzed (ASAS 475, 559, 673, and 866 nm, hereinafter labeled bands 1 through 4, respectively). The image signal-to-noise ratio for bands 1 through 3 was quite good (~100) but that in band 4 was markedly poorer, because of lower detector sensitivity. The band 4 image also had a coherent noise problem (noticeable periodic streaking appears in a herringbone pattern), mitigated somewhat by the averaging procedure, and a probable calibration problem, discussed later.

3. Aerosol Optical Depth Retrieval

To determine aerosol properties over land using passive remote sensing, it is necessary to have some information about the surface reflectance. If, for example, a large, dark water body exists within a scene, then the water pixel radiances can be interpreted mainly as atmospheric path radiance with only a small, correctable, component due to surface reflectance. Another surface type with presumed known reflectance properties is dense, dark vegetation (DDV), which will play a role in the analysis of EOS-MODIS data [*Kaufman et al.*, this issue] and also MISR data [*Diner et al.*, 1996a] to retrieve aerosol properties. For both dark water and DDV the reflectance is relatively small, allowing modest uncertainties to not unduly affect the accuracy of the aerosol retrieval. In general, however, surface reflectances within a scene are not usually known a priori, so other methods for treating surface reflectance must be investigated. Here two techniques are described which use the scene radiances directly and do not demand any additional information about the surface reflectance properties. However, these techniques cannot guarantee a useful aerosol retrieval for every scene to which they are applied because they both rely on the condition that there be a sufficient number of pixels which have different bihemispherical reflectances (albedos) but very similar directional reflectance shapes. The fact that an analysis of the directional characteristics of the observed radiance is at the heart of these techniques restricts their usage to multiangle imagery. Algorithms employing both techniques were used in the analysis of the ASAS data to retrieve aerosol optical depth.

3.1. Technique 1: Empirical Orthogonal Functions

An aerosol retrieval first was done using an algorithm based on a variation of the technique described by *Martonchik and Diner* [1992]. In the original version of the technique the images were operated upon by a fast Fourier transform (FFT) to generate power spectra as a function of spatial wavenumber and view angle. The angle-dependent power functions of the nonzero wavenumbers then were used to construct empirical orthogonal functions (EOFs) which described the spatially variable, angle dependent surface component of the observed radiance. These EOFs were used as basis vectors in an expansion of the surface component of the image-averaged radiance when an aerosol-ladened atmosphere model is introduced in the analysis. The best estimate of the aerosol optical depth is the model which minimized the residuals between the observed multiangle radiances and the corresponding model-dependent radiances, computed using the EOF-based surface radiance component.

The variation of the technique used in this study, and which is more closely related to the approach to be adopted with MISR, foregoes the FFT and constructs the EOFs directly from the radiances associated with the individual pixels in the images. To a good approximation the radiance $L_{x,y}^{\text{ASAS}}$ at the ASAS observation level can be written as

$$L_{x,y}^{\text{ASAS}}(-\mu,\ \mu_0,\ \phi-\phi_0) = L^{\text{atm}}(-\mu,\ \mu_0,\ \phi-\phi_0) + L_{x,y}^{\text{dir}}(-\mu,\ \mu_0,\ \phi-\phi_0) + L^{\text{dif}}(-\mu,\ \mu_0,\ \phi-\phi_0) \quad (1)$$

where L^{atm} is the radiance field scattered by the atmosphere up to the aircraft without interacting with the surface (i.e., the path radiance) and $L_{x,y}^{\text{dir}}$ and L^{dif} are the radiances directly and diffusely transmitted from the surface to the aircraft, respectively. $L_{x,y}^{\text{dir}}$ and L^{dif} can be expressed as

$$L_{x,y}^{\text{dir}}(-\mu,\ \mu_0,\ \phi-\phi_0) = \exp\,(-\tau/\mu)\,\frac{1}{\pi} \cdot \int_0^1\int_0^{2\pi} R_{x,y}(-\mu,\ \mu',\ \phi-\phi')L^{\text{inc}}(\mu',\ \mu_0,\ \phi'-\phi_0)\mu'\,d\mu'\,d\phi' \quad (2)$$

$$L^{\text{dif}}(-\mu,\ \mu_0,\ \phi-\phi_0) = \frac{1}{\pi}\int_0^1\int_0^{2\pi}\int_0^1\int_0^{2\pi} T(-\mu,\ -\mu'',\ \phi-\phi'') \cdot \bar{R}(-\mu'',\ \mu',\ \phi''-\phi')L^{\text{inc}}(\mu',\ \mu_0,\ \phi'-\phi_0)\mu'\,d\mu'\,d\phi'\,d\mu''\,d\phi'' \quad (3)$$

where x, y are the image pixel coordinates, μ and μ_0 are the cosines of the view and Sun angles, and $\phi - \phi_0$ is the view azimuth angle with respect to the Sun position. The convention $-\mu$ is used for upwelling radiation and μ for downwelling radiation. Also, τ is the optical depth of the atmosphere between the surface and the aircraft, L^{inc} is the radiance field incident on the surface, T is the upward diffuse atmospheric transmittance from the surface to the aircraft, $R_{x,y}$ is the spatially variable surface bidirectional reflectance factor (BRF), and $\bar{R}$ is the average surface BRF for the image. Note that only $L_{x,y}^{\text{dir}}$ is assumed spatially variable for the conditions of the ASAS observations. Similar expressions to (1), (2), and (3) also would describe the MISR observations except that both the direct and the diffuse radiation fields would be spatially variable.

The 64 × 64 pixel ASAS scene was subdivided into 4 × 4 subscenes, each with 16 × 16 pixels. Within each of these subscenes a separate aerosol optical depth retrieval was performed for each spectral band and the results for all subscenes then were averaged together. The EOFs required to implement the aerosol retrieval algorithm for each subscene are the eigenvectors associated with the real, symmetric scatter matrix constructed from reduced pixel radiances. Reduced pixel radiances are defined to be ASAS pixel radiances minus the pixel-averaged ASAS radiance, where the average is conducted over the subscene of 16 × 16 pixels. This subtraction process removes any effect of the atmospheric path radiance L^{atm} and the diffusely transmitted radiance L^{dif}, which are assumed to be the same for each pixel in the subscene. Thus each reduced pixel radiance $J_{x,y}$ at location x, y for each view angle is given by

$$J_{x,y}(-\mu,\ \mu_0,\ \phi-\phi_0) = L_{x,y}^{\text{ASAS}}(-\mu,\ \mu_0,\ \phi-\phi_0) - \langle L^{\text{ASAS}}(-\mu,\ \mu_0,\ \phi-\phi_0)\rangle = L_{x,y}^{\text{dir}}(-\mu,\ \mu_0,\ \phi-\phi_0) - \langle L^{\text{dir}}(-\mu,\ \mu_0,\ \phi-\phi_0)\rangle \quad (4)$$

where the operation angle brackets denote an average over all the pixels in the subscene. $J_{x,y}$, as expressed in (4), can be considered a linear combination of surface functions, $S_{x,y}$, defined to be that component of the measured radiance transmitted from the surface which is spatially variable. For ASAS observations,

$$S_{x,y}(-\mu,\ \mu_0,\ \phi-\phi_0) = L_{x,y}^{\text{dir}}(-\mu,\ \mu_0,\ \phi-\phi_0). \quad (5)$$

Following *Preisendorfer* [1988] the scatter matrix C can be written as

$$C_{ij} = \sum_{x,y} J_{x,y,i}J_{x,y,j}, \quad (6)$$

where subscripts i and j are now used to indicate the 10 different viewing geometries. The eigenvectors of C are solutions to the equation given by

$$\sum_{j=1}^{10} C_{ij}f_{n,j} = \lambda_n f_{n,i} \quad (7)$$

where λ_n is the eigenvalue (real and positive) of f_n. In general, there will be 10 eigenvalue and eigenvector solutions with the 10-element eigenvectors forming an orthonormal set; that is,

$$\sum_{i=1}^{10} f_{n,i}f_{m,j} = \delta_{nm}, \quad (8)$$

where δ_{nm} is the Kronecker symbol. Thus every 10-element vector $J_{x,y}$ can be expanded in terms of this orthonormal set as

$$J_{x,y,i} = \sum_{n=1}^{10} A_n^{x,y} f_{n,i} \tag{9}$$

where $A_n^{x,y}$ are the principal components,

$$A_n^{x,y} = \sum_{i=1}^{10} J_{x,y,i} f_{n,i}. \tag{10}$$

The eigenvectors are ordered according to the magnitude of the corresponding eigenvalues; that is, $\lambda_1 > \lambda_2 > \cdots > \lambda_{10}$. The set of vectors f_n is the optimum basis function set to represent the vectors $J_{x,y}$ in the sense that if only the first N ($N < 10$) eigenvectors are used in the expansion, then the resulting error e_N is a minimum when compared to the error using the first N vectors from a different vector basis function set. Here the error e_N is defined as

$$e_N = \sum_{x,y} \sum_{i=1}^{10} \left(J_{x,y,i} - \sum_{n=1}^{N} A_n^{x,y} \cdot f_{n,i} \right)^2$$

$$= \sum_{x,y} \sum_{i=1}^{10} \left(\sum_{n=N+1}^{10} A_n^{x,y} \cdot f_{n,i} \right)^2 = \sum_{n=N+1}^{10} \lambda_n. \tag{11}$$

Thus f_1 contributes most to the description of the vectors $J_{x,y}$ and f_{10} the least.

Now, as an example, if a single BRF shape is able to describe the view angle variability of the surface within a subscene (the individual pixel reflectances, however, being variable), then the reduced pixel radiances are proportional to each other; that is,

$$J_{x,y,i} = c' J_{x',y',i} = c f_{1,i}. \tag{12}$$

In this particular case, the scatter matrix C has rank 1 and the resulting single EOF, f_1, is proportional to $J_{x,y}$, this being a limiting form of (9). If the correct atmospheric path radiance L^{atm} and diffusely transmitted radiance L^{dif} are subtracted from the pixel-averaged ASAS radiance, then the resulting pixel-averaged surface function also must be proportional to f_1; that is,

$$\langle L_i^{\text{ASAS}} \rangle - L_i^{\text{atm}} - L_i^{\text{dif}} = \langle L_i^{\text{dir}} \rangle = \langle S_i \rangle = a_1 f_{1,i} \tag{13}$$

When knowledge of the correct atmospheric state is not known, (13) then can be used as a criterion to determine the best estimate of the atmospheric state (i.e., aerosol optical depth) by requiring that it produce the minimum deviation D_1 in angular shape between $\langle L^{\text{ASAS}} \rangle - L^{\text{atm}} - L^{\text{dif}}$ and f_1. This can be written as

$$D_1(\text{model}, \tau_{\text{aer}}) = \sum_{i=1}^{10} (\langle L_i^{\text{ASAS}} \rangle - L_i^{\text{atm}}(\text{model}, \tau_{\text{aer}}) - L_i^{\text{dif}}(\text{model}, \tau_{\text{aer}}) - a_1 f_{1,i})^2 \tag{14}$$

where the summation is over the ASAS view angles, L_i^{atm} and L_i^{dif} are model-generated radiances at a given aerosol optical depth τ_{aer} and a_1 is obtained from the general expression

$$a_n = \sum_{i=1}^{10} (\langle L_i^{\text{ASAS}} \rangle - L_i^{\text{atm}}(\text{model}, \tau_{\text{aer}}) - L_i^{\text{dif}}(\text{model}, \tau_{\text{aer}})) f_{n,i}. \tag{15}$$

The computation of L_i^{dif} requires that the average surface BRF, $\bar{R}$, for the scene be known or estimated, as indicated in (3). An estimate of $\bar{R}$, however, can be readily obtained by means of the surface retrieval algorithm described in the following section, using the aerosol model and optical depth being tested. When the algorithm is applied to MISR data, the computation of L_i^{dif} is not necessary since it is assumed to be spatially variable and therefore is considered with $L_{x,y}^{\text{dir}}$ as a component of the surface functions $S_{x,y}$. As such, it is represented along with $L_{x,y}^{\text{dir}}$ by the EOFs.

When more than one BRF shape are represented in the subscene, then (14) is no longer rigorously satisfied. However, since $\langle L^{\text{ASAS}} \rangle - L^{\text{atm}} - L^{\text{dif}}$, like $J_{x,y}$, is made up of a linear combination of surface functions $S_{x,y}$, it is desirable to expand it using the EOFs, f_n. Therefore

$$\langle L_i^{\text{dir}} \rangle = \langle S_i \rangle \cong \sum_{n=1}^{N} a_n f_{n,i} \tag{16}$$

and (14) can be generalized to

$$D_1(\text{model}, \tau_{\text{aer}}) = \sum_{i=1}^{10} \left(\langle L_i^{\text{ASAS}} \rangle - L_i^{\text{atm}}(\text{model}, \tau_{\text{aer}}) - L_i^{\text{dif}}(\text{model}, \tau_{\text{aer}}) - \sum_{n=1}^{N} a_n f_{n,i} \right)^2 \tag{17}$$

where $N < 10$ and the expansion coefficients a_n again are obtained from (15). As an extension of (14), this expression assumes that there are a few different BRF shapes present within the subscene but each having a variety of reflectances. Because of the ordering of the eigenvalues, a cutoff in the summation of (17) is invoked, using only those eigenvectors with an eigenvalue λ_n greater than 0.05 λ_1. This condition effectively defines the maximum value of N, N_{max} with the constraint that N_{max} also be less than the total number of eigenvectors. In practice, N_{max} should not exceed 3 or 4 since each additional eigenvector used in the expansion described in (17) implies a corresponding decrease in sensitivity to the various aerosol models being investigated.

For a given candidate aerosol model a D_1 is computed for each value of N used in (17), starting with $N = 1$ (the first eigenvector only) up through N_{max}. Varying the model aerosol optical depth, the minimum D_1 for each N, D_1^N, defines an estimate of the optical depth τ_N. The best estimate is defined as a weighted average of all N_{max} optical depths,

$$\tau_{\text{best}} = \left(\sum_{N=1}^{N_{\text{max}}} \frac{1}{D_1^N} \cdot \tau_N \right) \Bigg/ \left(\sum_{N=1}^{N_{\text{max}}} \frac{1}{D_1^N} \right), \tag{18}$$

and the weights are the inverses of the D_1^N. The effective D_1 associated with τ_{best} is defined as the weighted average of the D_1^N,

$$\frac{1}{D_1^{\text{eff}}} = \frac{1}{N} \cdot \sum_{N=1}^{N_{\text{max}}} \frac{1}{D_1^N}. \tag{19}$$

A τ_{best} and a D_1^{eff} are determined for each of the 16 subscenes and used to compute a weighted average optical depth and variance for the scene, with the weights defined as the inverses of the D_1^{eff}.

3.2. Technique 2: Similar Surface Types

It is instructive to contrast the EOF technique, described above, with a relatively less efficient but conceptually simpler one, based on similar principles. The technique is to explicitly search for pixels which have the same (or closely similar) surface directional reflectance shapes but different bihemispherical reflectances (albedos). Comparison of unique pixel pairs, however, rapidly becomes a very time consuming process with increasing size of the comparison area in the image.

For two pixels with similar directional reflectances, labeled 1 and 2, the criterion

$$L_{1,i}^{\mathrm{ASAS}} - L_i^{\mathrm{atm}} - L_i^{\mathrm{dif}} = b(L_{1,i}^{\mathrm{ASAS}} - L_{2,i}^{\mathrm{ASAS}}), \quad (20)$$

where b is a constant of proportionality, is satisfied for the correct atmospheric state described by L_i^{atm} and L_i^{dif}. When searching for the correct atmospheric state, (20) can be incorporated into an expression describing the goodness of fit,

$$D_2(\mathrm{model}, \tau_{\mathrm{aer}}) = \sum_{\mathrm{pairs}} \sum_{i=1}^{10} [L_{1,i}^{\mathrm{ASAS}} - L_i^{\mathrm{atm}}(\mathrm{model}, \tau_{\mathrm{aer}}) - L_i^{\mathrm{dif}}(\mathrm{model}, \tau_{\mathrm{aer}}) - b(L_{1,i}^{\mathrm{ASAS}} - L_{2,i}^{\mathrm{ASAS}})]^2, \quad (21)$$

where b is determined by least squares. The same subdivision scheme (4 × 4 subscenes) of the ASAS image was also used with this technique, resulting in 32640 unique pixel pairs per subscene. For a given model, it is assumed that the optical depth τ_{aer} which produces the minimum value of D_2 is the best estimate of the subscene aerosol optical depth. The best estimate of subscene optical depths are then averaged together as is done for the EOF retrieval technique.

If every pixel is unique in its angular reflectance properties, then D_2 is expected to be insensitive to the various atmospheric models being tested and this technique will probably fail.

3.3. Aerosol Analysis of Glacier NP ASAS Data

The aerosol model used in the analysis was assumed to be clean, continental, composed mainly of submicron size water-soluble sulfates and nitrates [*d'Almeida et al.*, 1991]. These types of aerosol particles are generally consistent with in situ measurements made over rural, interior, medium-latitude regions of North America [e.g., *Hobbs et al.*, 1988]. For computational purposes the aerosols were assumed to have a scale height of 1 km within a Rayleigh scattering molecular atmosphere. The multiple scattering, radiative transfer code was a discrete-ordinate, matrix operator type [*Grant and Hunt*, 1968] which can account for surfaces with non-Lambertian reflectance properties. The model radiances, required by the retrieval algorithms, were computed for various aerosol optical depths, given the appropriate solar angle and view angles, elevation of the scene, and altitude of the observations.

The aerosol optical depth results for the four selected ASAS spectral channels and for the two retrieval techniques are shown in Figure 2. Both techniques give essentially the same results, an optical depth of about 0.03 ± 0.02 at 555 nm, indicating a very light aerosol loading. Also shown is the spectral dependence of the aerosol model, visually scaled to the retrieval results. Apart from the results at 866 nm, the model spectral dependence is consistent with the retrieval results, validating to some degree the choice of the model. The optical depths at 866 nm are larger than expected and show considerably more uncertainty than those at the other wavelengths, a consequence of the larger amounts of random and systematic noise in the imagery and a probable calibration problem, discussed later, which resulted in multiangle radiances that are too large. By the nature of the algorithm, a serious calibration problem in any spectral band would affect the associated aerosol optical depth retrieval in a way that cannot readily be anticipated. However, it is not unreasonable to expect that at least a portion of this excess radiance would translate into a larger than expected optical depth.

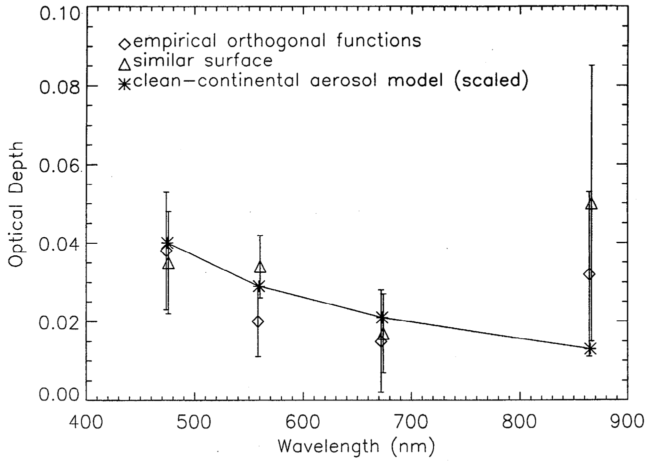

Figure 2. Retrieved aerosol optical depth.

4. Surface Reflectance Retrieval

Once the atmospheric properties are known, the surface reflectance retrieval is accomplished in a straightforward manner. Since the diffuse radiance at the aircraft level is considered to be spatially invariant over the scene, it is computed first. The retrieval process starts by pixel-averaging the ASAS full scene radiance and retrieving the pixel-averaged surface-leaving radiance. Using (1) through (3), the pixel-averaged ASAS radiance can be written as

$$\begin{aligned}
&\langle L^{\mathrm{ASAS}}(-\mu, \mu_0, \phi - \phi_0)\rangle \\
&= L^{\mathrm{atm}}(-\mu, \mu_0, \phi - \phi_0) + \langle L^{\mathrm{dir}}(-\mu, \mu_0, \phi - \phi_0)\rangle \\
&\quad + L^{\mathrm{dif}}(-\mu, \mu_0, \phi - \phi_0) \\
&= L^{\mathrm{atm}}(-\mu, \mu_0, \phi - \phi_0) \\
&\quad + \exp(-\tau/\mu) L^{\mathrm{surf}}(-\mu, \mu_0, \phi - \phi_0) \\
&\quad + \int_0^1 \int_0^{2\pi} T(-\mu, -\mu', \phi - \phi') L^{\mathrm{surf}}(-\mu', \mu_0, \phi' - \phi_0)\, d\mu'\, d\phi',
\end{aligned} \quad (22)$$

where the pixel-averaged surface-leaving radiance L^{surf} is

$$L^{\mathrm{surf}}(-\mu, \mu_0, \phi - \phi_0) = \frac{1}{\pi} \int_0^1 \int_0^{2\pi} \bar{R}(-\mu, \mu', \phi - \phi') L^{\mathrm{inc}}(\mu', \mu_0, \phi' - \phi_0) \mu'\, d\mu'\, d\phi'. \quad (23)$$

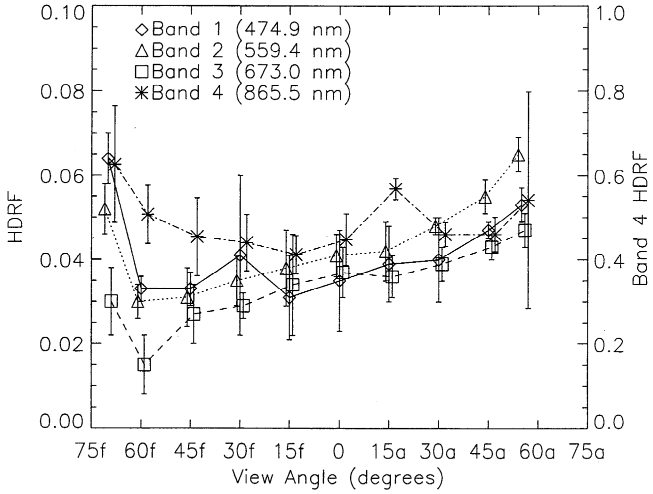

Figure 3. Retrieved hemispherical-directional reflectance factor (HDRFs) for conifer canopy. Note the change in scale for band 4.

The integral equation of (22) can be easily solved for L^{surf} using an iterative approach, once the model generated L^{atm}, τ, and T are defined [*Diner et al.*, 1996b]. Following the determination of L^{surf}, the diffusely transmitted radiance L^{dif} (the last term in (22)) can be computed. Recall that L^{dif} also was needed when performing the aerosol retrieval. Once L^{dif} is determined, $L^{\text{dir}}_{x,y}$ the directly transmitted radiance for each pixel then can be calculated using (1). The surface-leaving radiance $L^{\text{surf}}_{x,y}$ is directly related to $L^{\text{dir}}_{x,y}$; that is,

$$L^{\text{surf}}_{x,y}(-\mu, \mu_0, \phi - \phi_0) = L^{\text{dir}}_{x,y}(-\mu, \mu_0, \phi - \phi_0)/\exp(-\tau/\mu). \tag{24}$$

The surface hemispherical-directional reflectance factor (HDRF), $r_{x,y}$, for each pixel is obtained by ratioing $L^{\text{surf}}_{x,y}$ to the surface-leaving radiance from an ideal Lambertian surface, $L^{\text{surf}}_{\text{lam}}$. The isotropic radiance $L^{\text{surf}}_{\text{lam}}$ is determined from the expression

$$L^{\text{surf}}_{\text{lam}} = \frac{1}{\pi}\int_0^1\int_0^{2\pi} L^{\text{inc}}(\mu', \mu_0, \phi' - \phi_0)\mu'\, d\mu'\, d\phi'$$

$$\cong \frac{1}{1 - s\langle\rho\rangle}\cdot\frac{1}{\pi}\int_0^1\int_0^{2\pi} L^{\text{inc}}_0(\mu', \mu_0, \phi' - \phi_0)\mu'\, d\mu'\, d\phi' \tag{25}$$

where L^{inc}_0 is the incident radiance on a black surface, s is the bottom-of-atmosphere bihemispherical reflectance, and $\langle\rho\rangle$ is the full scene-averaged surface reflectance, all readily computed. Integration of the HDRF $r_{x,y}$ over the viewing hemisphere results in the bihemispherical reflectance (BHR) $\rho_{x,y}$ or albedo. Since $r_{x,y}$ is computed only at the ASAS view angles, this integration is accomplished by assuming that it can be expressed as a two-term expansion in $\phi - \phi_0$. Thus

$$r_{x,y}(-\mu, \mu_0, \phi - \phi_0) = L^{\text{surf}}_{x,y}(-\mu, \mu_0, \phi - \phi_0)/L^{\text{surf}}_{\text{lam}}$$

$$\cong r_{0,x,y}(-\mu, \mu_0) + r_{1,x,y}(-\mu, \mu_0)\cos(\phi - \phi_0) \tag{26}$$

$$\rho_{x,y}(\mu_0) = 2\int_0^1\int_0^{2\pi} r_{0,x,y}(-\mu, \mu_0, \phi - \phi_0)\mu\, d\mu \tag{27}$$

Surface HDRF results are shown in Figure 3 for the conifer forest and in Figure 4 for the snow- and ice-covered lake. The corresponding BHR results are listed in Table 1. To consolidate the results, similar surface pixel types were averaged together for both the forest and the lake. The vertical bars in the figures indicate the range of variability over the scene for each surface type. This variability is due in part to actual pixel-to-pixel surface differences (i.e., spotted vegetation or lake snow conditions), evident within the scene, and also to image noisiness. Band 4 results in particular for both the forest and the lake are about 5 to 10 times more noisy than the other bands, as evidenced in Figure 4 and Table 1.

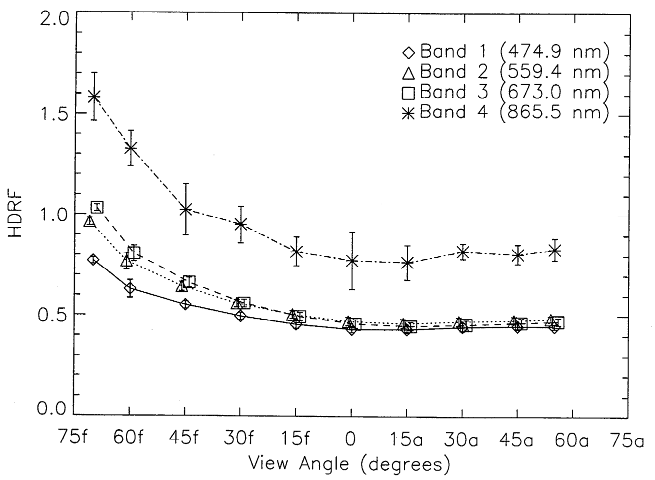

Figure 4. Retrieved HDRFs for snow- and ice-covered Bowman Lake.

5. Discussion

The HDRF variation with view angle for the conifer forest shows both forward and backward scattering, resulting in a bowl shape which is typical of this kind of vegetation [*Kimes*, 1983; *Kimes et al.*, 1985]. The spectral dependence of the BHR for the forest is representative of dense, dark vegetation, i.e., low (<0.05) at visible wavelengths due mainly to chlorophyll absorption and high in the near infrared. The BHR in band 4 equal to 0.49, however, appears too high for this type of canopy. The measurements of *Kimes* [1983] and *Kimes et al.* [1985] indicate that it should be in the neighborhood of 0.3. It might seem probable that any snow-covered ground between the trees would increase the BRF to the observed level. However, this does not seem to be the case because the visible bands do

Table 1. Scene BHR

Band	Forest	Lake
1	0.048 ± 0.005	0.52 ± 0.01
2	0.050 ± 0.004	0.57 ± 0.01
3	0.042 ± 0.005	0.58 ± 0.01
4	0.49 ± 0.06	0.97 ± 0.03

BHR, bihemispherical reflectance.

not appear to be affected. Even the HDRF at nadir view indicates no significant presence of a snow ground cover, a condition also observed by *Hall et al.* [1993] in ASAS data taken at a neighboring region around St. Mary Lake.

The HDRF variation with view angle for the lake shows moderate forward scattering, increasing slightly with wavelength, in agreement with the observations of *Salomonson and Marlatt* [1968] for snow. The spectral dependence of the BHR for a clean snow and ice-covered lake should be fairly uniform across visible wavelengths with values near unity and a downturn in the near IR with amount depending on grain size [*Warren and Wiscombe*, 1980]. However, bands 1 through 3 have BHR values about 0.55, suggesting that the snow cover is contaminated, and band 4 has a BHR value near unity. Calculations by *Warren and Wiscombe* [1980] indicate that soot contamination of the snow of only a few ppmw can reduce the BHR values in the visible to those in Table 1 and produce a band 4 BHR value about equal to that of band 3. Assuming this contamination scenario to be valid, this again implies that the band 4 BRF result is too high, as it was for the forest. To bring the band 4 BHR values of the two surface types down to their expected values requires a correction factor of about 0.6 applied to the radiances, implying that the calibration coefficient for this channel is too high by about 67%. Since Table 1 shows that the lake BHR has a spectral shape similar to that of the forest an alternative contamination possibility is that dead needles from the conifers were strewn about on the snow surface. To lower the visible BHR of the snow to 0.55 requires that over 40% of the surface was needle litter. If no adjustment is made in the calibration of band 4 and the BHR for conifers in that band is taken as 0.49 then the band 4 BHR for the snow would be 1.33, well in excess of the theoretical limit. Again, if a calibration correction of 0.6 is applied to the radiances of band 4, then the BRF for snow in that band would be 0.79, in general agreement with the models of Warren and Wiscombe. Thus both the soot and the needle litter scenarios require that band 4 radiances be reduced by about the same amount, allowing a mixing of both types of contamination as another possibility. A large error in the calibration of band 4 (866 nm) is not unreasonable, due to the relatively poor response and nonlinearity of the ASAS detectors for wavelengths longer than 770 nm [*Irons*, 1991]. This CID detector array has since been replaced by a more sensitive CCD array.

When measurements are made with ASAS, it is desirable to have coincident field measurements acquired within the imaged scene to compare with the aircraft results. There was some sunphotometer data taken, but it was not of sufficient quality to validate the small amount of aerosol retrieved from the ASAS data. Some reflectance data were also obtained on the lake, but instrument calibration problems have not allowed the data to be properly analyzed to date (D. K. Hall, personal communication, 1996).

The approach used here to analyze the multiangle image data sets from ASAS is part of the overall strategy for MISR data analysis over land. The aerosol optical depth retrieval technique, using empirical orthogonal functions to describe the surface directional reflectance, is the third option in a hierarchy of aerosol retrieval algorithms that will be used on MISR data. The hierarchy is based on the amount of information known for a surface type within a scene or region. The first option is the algorithm which requires that the surface reflectance properties be completely known at one or more MISR wavelengths. The only surface type that fits this category at present is a dark water body, exemplified by a large, deep, permanent inland lake. After MISR has been flying for a period of time, it is expected that more land surface types (e.g., selected desert areas) will be added to the list. The second option is an algorithm used for those surface types which are completely defined except for one parameter. It is anticipated that by launch time, dense, dark vegetation at the blue and red MISR wavelengths will be in this category. Work is currently under way to characterize these vegetation models using AVHRR data (Verstraete, personal communication, 1995) and additional testing will be done using ASAS data. The third option, the algorithm described in this paper, assumes virtually nothing about the surface types within a region but requires that sufficient contrast (variable reflectance or albedo) be available. As such, this algorithm requires more extensive testing and validation than the other two. The ASAS data analyzed in this paper are part of a series of ASAS imagery which is available and which will be analyzed in the context of the aerosol algorithm hierarchy.

The described surface reflectance retrieval algorithm takes advantage of the multiangle nature of the data by incorporating the non-Lambertian character of the surface directly into the retrieval process. As such it is a more accurate procedure than assuming the surface acts as a Lambertian scatterer with a view-dependent albedo [e.g., *Ranson et al.*, 1994]. The process of testing and validating the surface retrieval algorithm will also be achieved through the continuing analysis of ASAS data, with the retrieved surface directional reflectance properties being compared to available field data. Furthermore, an airborne MISR simulator (AirMISR) instrument is currently being fabricated at the Jet Propulsion Laboratory, and preliminary science flights are scheduled for early 1997. This instrument will play a key role in the continuing algorithm development and validation program for the MISR project. Additional information about the MISR aerosol and surface retrieval algorithms and the resulting geophysical products can be found in the MISR algorithm theoretical basis documents [*Diner et al.*, 1996a, b].

Acknowledgments. I thank J. Irons and D. Hall of the Goddard Space Flight Center for providing the ASAS imagery and L. Barge and B. Rheingans for coregistering the multiangle images. I also thank B. Rheingans for the graphical work and L. Travis, Y. Kaufman, D. Diner, R. Kahn, and R. West and for careful reviews of the manuscript. This research was performed by the Jet Propulsion Laboratory, California Institute of Technology, under contract with the National Aeronautics and Space Administration.

References

Charney, J. G., W. G. Quirk, S. M. Chow, and J. Kornfield, A comparative study of the effects of albedo change of drought in semi-arid regions, *J. Atmos. Sci.*, *34*, 1366–1385, 1977.

d'Almeida, G. A., P. Koepke, and E. P. Shettle, *Atmospheric Aerosols: Global Climatology and Radiative Characteristics*, 561 pp., A. Deepak, Hampton, Va., 1994.

Dickinson, R. E., Land surface processes and climate-surface albedos and energy balance, *Adv. Geophys.*, *25*, 305–353, 1983.

Diner, D. J., C. J. Bruegge, J. V. Martonchik, G. W. Bothwell, E. D. Danielson, E. L. Floyd, V. G. Ford, L. E. Hovland, K. L. Jones, and M. L. White, A multi-angle imaging spectroradiometer for terrestrial remote sensing from the Earth Observing System, *Int. J. Imaging Syst. Technol.*, *3*, 92–107, 1991.

Diner, D. J., et al., MISR level 2 aerosol retrieval algorithm theoretical basis, *JPL D-11400, Rev. B*, Jet Propul. Lab., Pasadena, Calif., 1996a.

Diner, D. J., J. V. Martonchik, C. Borel, S. A. W. Gerstl, H. R. Gordon, R. Myneni, S. R. Paradise, B. Pinty, and M. Verstraete, MISR level 2 surface retrieval algorithm theoretical basis, *JPL D-11401, Rev. B*, 1996b.

Grant, I. P., and G. E. Hunt, Solution of radiative transfer problems using the invariant S_n method, *Mon. Not. R. Astron. Soc.*, *141*, 27–41, 1968.

Hall, D. K., J. L. Foster, J. R. Irons, and P. W. Dabney, Airborne bidirectional radiances of snow-covered surfaces in Montana, U.S.A., *Ann. Glaciol.*, *17*, 35–40, 1993.

Hobbs, P. V., J. H. Lyons, and L. F. Radke, Background particle size distributions over North America, in *Atmospheric Aerosols and Nucleation*, edited by P. E. Wagner and G. Vali, pp. 217–220, Springer-Verlag, New York, 1988.

Irons, J. R., K. J. Ranson, D. L. Williams, R. R. Irish, and F. G. Huegel, An off-nadir-pointing imaging spectroradiometer for terrestrial ecosystem studies, *IEEE Trans. Geosci. Remote Sens.*, *29*, 66–74, 1991.

Kaufman, Y. J., D. Tanré, L. Remer, E. Vermote, A. Chu, and B. N. Holben, Operational remote sensing of tropospheric aerosol over the land from EOS moderate resolution imaging spectroradiometer, *J. Geophys. Res.*, this issue.

Kimes, D. S., Dynamics of directional reflectance factor distributions for vegetation canopies, *Appl. Opt.*, *22*, 1364–1372, 1983.

Kimes, D. S., W. W. Newcomb, R. F. Nelson, and J. B. Schutt, Directional reflectance distributions of a hardwood and pine forest canopy, *IEEE Trans. Geosci. Remote Sens.*, *GE-24*, 281–293, 1985.

Martonchik, J. V., and D. J. Diner, Retrieval of aerosol optical properties from multi-angle satellite imagery, *IEEE Trans. Geosci. Remote Sens.*, *30*, 223–230, 1992.

Mintz, Y., The sensitivity of numerically simulated climates to land-surface conditions, in *The Global Climate*, edited by J. Houghton, pp. 79–105, Cambridge University Press, New York, 1984.

Preisendorfer, R. W., *Principal Component Analysis in Meteorology and Oceanography*, 425 pp., Elsevier, New York, 1988.

Ranson, K. J., J. R. Irons, and D. L. Williams, Multispectral bidirectional reflectance of northern forest canopies with the Advanced Solid-State Array Spectroradiometer (ASAS), *Remote Sens. Environ.*, *47*, 276–289, 1994.

Salomonson, V. V., and W. E. Marlatt, Anisotropic solar reflectance over white sand, snow and stratus cloud, *J. Appl. Meteorol.*, *7*, 475–483, 1968.

Warren, S. G., and W. J. Wiscombe, A model for the spectral albedo of snow, II, Snow containing atmospheric aerosols, *J. Atmos. Sci.*, *37*, 2734–2745, 1980.

J. Martonchik, Jet Propulsion Laboratory, CIT, MS 169-237, 4800 Oak Grove Drive, Pasadena, CA 91109.

(Received February 21, 1996; revised June 19, 1996; accepted July 24, 1996.)